

# RigNet: Repetitive Image Guided Network for Depth Completion

Zhiqiang Yan<sup>1</sup>, Kun Wang<sup>1</sup>, Xiang Li<sup>1</sup>, Zhenyu Zhang<sup>1</sup>, Baobei Xu<sup>2,3</sup>, Jun Li<sup>1\*</sup>, Jian Yang<sup>1\*</sup>

<sup>1</sup>PCA Lab, Nanjing University of Science and Technology

<sup>2</sup>Hikvision Research Institute <sup>3</sup>Zhejiang University

{Yanzq, kunwang, xiang.li.implus, junli, csjyang}@njust.edu.cn,

zhangjesse@foxmail.com, 21625177@zju.edu.cn

## Abstract

*Depth completion deals with the problem of recovering dense depth maps from sparse ones, where color images are often used to facilitate this completion. Recent approaches mainly focus on image guided learning to predict dense results. However, blurry image guidance and object structures in depth still impede the performance of image guided frameworks. To tackle these problems, we explore a repetitive design in our image guided network to sufficiently and gradually recover depth values. Specifically, the repetition is embodied in a color image guidance branch and a depth generation branch. In the former branch, we design a repetitive hourglass network to extract higher-level image features of complex environments, which can provide powerful context guidance for depth prediction. In the latter branch, we design a repetitive guidance module based on dynamic convolution where the convolution factorization is applied to simultaneously reduce its complexity and progressively model high-frequency structures, e.g., boundaries. Further, in this module, we propose an adaptive fusion mechanism to effectively aggregate multi-step depth features. Extensive experiments show that our method achieves state-of-the-art result on the NYUv2 dataset and ranks 1st on the KITTI benchmark at the time of submission.*

## 1. Introduction

Depth completion, the technique of converting sparse depth measurements to dense ones, has a variety of applications in the computer vision field, such as autonomous driving [13, 6], augmented reality [7, 40], virtual reality [1], and 3D scene reconstruction [52, 35]. The success of these applications heavily depends on reliable depth predictions. Recently, multi-modal information from various sensors is involved to help generate dependable depth results, such as color images [32, 2], surface normals [52, 37], confidence maps [9, 44], and even binaural echoes [11, 34]. Particularly, the latest image guided methods [54, 28, 16, 42] prin-

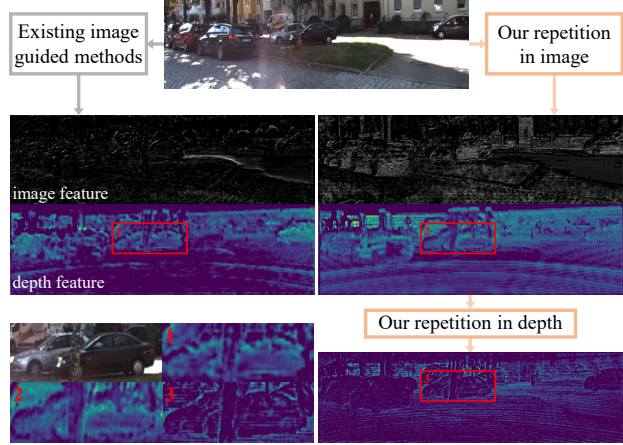


Figure 1. Image and depth features comparison between the existing image guided methods and our repetitive model. Our repetitive designs produce image features that have much clearer and richer contexts than others, while our depth features not only have denser contents, but also detailed structures.

cipally concentrate on using color images to guide the recovery of dense depth maps, achieving outstanding performance. However, due to the challenging environments and limited depth measurements, it's difficult for existing image guided methods to produce clear image guidance and structure-detailed depth features. To deal with these problems, in particular, we deploy a novel repetitive design in both the image guidance and depth generation branches.

In the image guidance branch: As shown in the left image feature of Fig. 1, existing image guided methods are not sufficient to produce very precise details to provide perspicuous image guidance. Such blurry guidance has a negative impact on the content-complete depth recovery. Since higher-level convolutional layers possess greater invariance and exaggeration in discriminative parts of images [49], we present a repetitive hourglass network which repeatedly stacks same units to further produce higher-level image semantics. As obviously illustrated in Fig. 1, our image feature has much clearer and richer contexts than that of previous image guided methods. Owing to the high-quality im-

age guidance, the corresponding depth feature has denser depth pixels and more complete object shapes. The detailed comparison can be found in red boxes 1 and 2 in Fig. 1.

In the depth generation branch: It is known that gradients near boundaries usually have large mutations, which increase the difficulty of recovering structure-detailed depth for convolution [43]. For example, as shown in the left depth feature of Fig. 1, we can observe that the boundaries are not very clear, where the depth values are usually hard to predict [17, 9, 35]. Since the gradual refined strategy [4, 3, 47, 35] is beneficial to model depth boundaries, in the depth generation branch, we propose a repetitive guidance module based on dynamic convolution [42] to moderate the issue, which first extracts the high-frequency components (*e.g.*, depth boundaries) by channel-wise and cross-channel convolution factorization, and then progressively produces refined depth by repeatedly stacking the guidance units. We also design an adaptive fusion mechanism to effectively study better depth representations by aggregating depth features of each repetitive unit. However, an obvious drawback of the dynamic convolution operation using spatial-variant kernels is the large GPU memory consumption, especially under the case of repetitive structure. Therefore, based on a simplified implementation of dynamic convolution [42], we further design an efficient guidance algorithm to implement our lightweight multi-stage feature learning. Finally, as illustrated in Fig. 1, our depth feature in red box 3 has sharper structure than that in red box 1.

Benefiting from the clearer image contexts and depth structures, our model can recover more accurate depth details in challenging environments, which are shown in Figs. 1, 4 and 5. In short, our contributions are in three aspects:

- We propose the novel repetitive hourglass network, which can extract legible image features of challenging environments to provide clearer guidance for depth recovery.
- We present the novel repetitive guidance module based on dynamic convolution, including an adaptive fusion mechanism and an efficient guidance algorithm, which can gradually learn precise depth representations.
- Extensive experimental results demonstrate the effectiveness of our method. Our model achieves state-of-the-art performance on both the outdoor KITTI benchmark and the indoor NYUv2 dataset.

## 2. Related Work

**Depth only approaches.** The task of depth completion has caused wide public concern in computer vision and robotics since the work [43] proposes sparsity invariant CNNs to deal with sparse depth input for the first time. After ResNets [14] come along, a simple framework applied to the task is conducting a single U-net [38], which usually

uses ResNets as encoder. On this basis, the early depth completion methods [43, 23, 5, 21, 9, 32, 45] mainly input depth maps without the corresponding color images. Further, Lu *et al.* [30] take sparse depth as the only input with color images being auxiliary supervision. However, single-modal based depth completion methods are limited without other information as reference. As the technology quickly develops, lots of multi-modal information is available, which can greatly facilitate the depth completion task.

**Image guided methods.** Existing image guided depth completion methods can be roughly divided into two patterns. One pattern is that RGB-D concatenations are directly input into a single symmetrical hourglass network [32, 4, 2, 3, 35, 47]. For example, S2D [32] directly feeds the concatenation of a sparse depth and its corresponding color image into a simple Unet [38]. FuseNet [2] designs an effective block that learns to extract joint 2D and 3D features. CSPN [4] studies the affinity matrix to refine coarse depth maps with spatial propagation network (SPN) at the end of its Unet. CSPN++ [3] further improves its effectiveness and efficiency by learning adaptive convolutional kernel sizes and the number of iterations for propagation. NLSPN [35] further utilizes their non-local SPN which effectively avoids irrelevant local neighbors and focuses on relevant non-local neighbors during propagation. DSPN [47] proposes a deformable SPN to adaptively generates different receptive field and affinity matrix at each pixel for effective propagation. Another pattern is using two independent branches to extract the color image and depth features respectively and then fuse them at multi-scale stages [44, 48, 42, 25, 28, 16]. For example, PENet [16] employs feature addition to guide depth learning at different stages. FCFRNet [28] proposes channel-shuffle technology to enhance RGB-D feature fusion. ACMNet [54] chooses to adopt the graph propagation to capture the observed spatial contexts in the encoder stage. Although these methods conduct image guidance strategy in the whole networks, they naïvely fuse the multi-modal RGB-D information by simple addition or concatenation. Differently, GuideNet [42] seeks to predict dynamic kernel weights from the guided image and then the weights are applied to adaptively extract the depth features, which greatly improves the performance of double-branch models. All these image guided approaches can provide specific directions for further promoting the performance of the depth completion task.

**Repetitive learning models.** To extract more accurate and abundant feature representations, many approaches propose to repeatedly stack similar components. For example, PANet [29] adds an extra bottom-up path aggregation which is similar with its former top-down feature pyramid network (FPN). NAS-FPN [12] and BiFPN [41] conduct repetitive blocks to sufficiently encode discriminative image semantics for object detection. FCFRNet [28] argues that

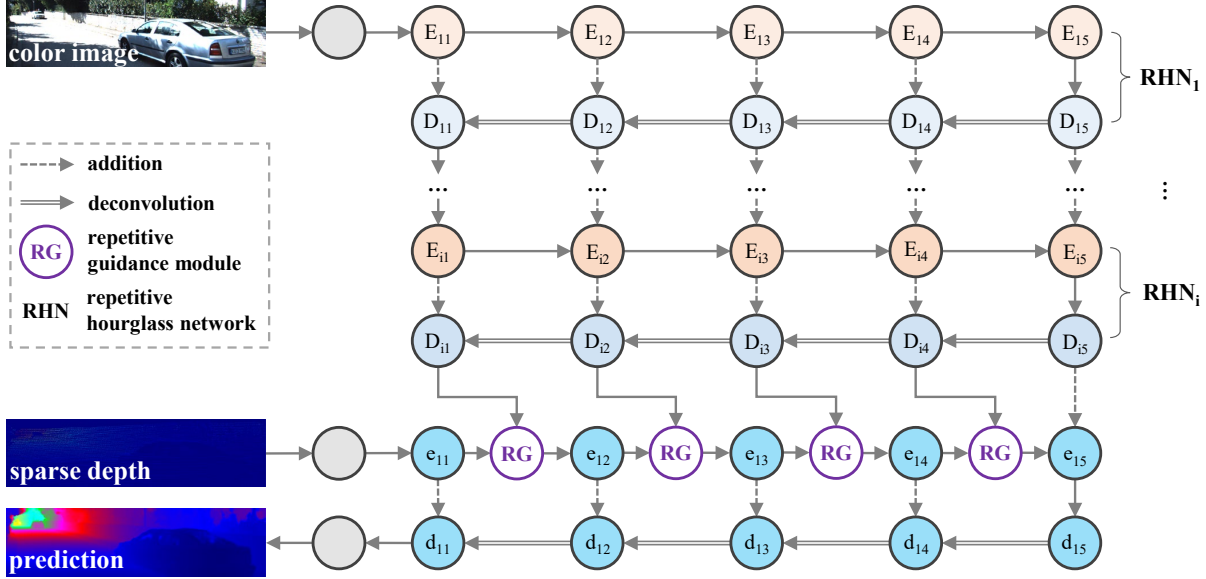


Figure 2. Overview of our repetitive image guided network. The pipeline contains an image guidance branch and a depth generation branch. The former consists of a repetitive hourglass network and the latter has the same structure as  $RHN_1$ . In the depth branch, we perform our novel repetitive guidance module (elaborated in Fig. 3) to refine depth. In addition, an efficient guidance algorithm and an adaptive fusion mechanism are proposed to further improve the performance of the module.

the feature extraction in one-stage frameworks are insufficient. They formulate the depth completion as a two-stage learning task, where the final output of the sparse-to-coarse stage is transported to the coarse-to-fine stage. Such design can be seen as basic component repetition. On this basis, PENet [16] further improves its performance by utilizing confidence maps and varietal CSPN++. Different from these methods, in our image branch we first conduct repetitive CNNs units to produce clear guidance features at multi-scale layers. Then in our depth branch we perform repetitive guidance module to generate structure-detailed depth.

### 3. Repetitive Design

In this section, we first introduce our repetitive hourglass network (RHN), then elaborate the proposed repetitive guidance module (RG), including an efficient guidance algorithm (EG) and an adaptive fusion mechanism (AF).

#### 3.1. Repetitive Hourglass Network

For autonomous driving in challenging environments, it is important to understand the semantics of color images in view of the sparse depth measurement. The problem of blurry image guidance can be mitigated by a powerful feature extractor, which can obtain context-clear semantics. In this paper we present our repetitive hourglass network shown in Fig. 2.  $RHN_i$  is a symmetrical hourglass unit like Unet. The original color image is first encoded by a  $5 \times 5$  convolution and then input into  $RHN_1$ . Next, we repeatedly utilize the same unit to gradually extract high-level semantics. In the encoder of  $RHN_i$ ,  $E_{ij}$  takes  $E_{i(j-1)}$  and

$D_{(i-1)j}$  as input. In the decoder of  $RHN_i$ ,  $D_{ij}$  inputs  $E_{ij}$  and  $D_{i(j+1)}$ . The process can be defined as:

$$E_{ij} = \begin{cases} Conv(D_{(i-1)j}), & j = 1, \\ Conv(E_{i(j-1)}) + D_{(i-1)j}, & 1 < j \leq 5, \end{cases} \quad (1)$$

$$D_{ij} = \begin{cases} Conv(E_{i5}), & j = 5, \\ Deconv(D_{i(j+1)}) + E_{ij}, & 1 \leq j < 5, \end{cases}$$

where  $Conv(\cdot)$  and  $Deconv(\cdot)$  represent convolution and deconvolution functions respectively.

#### 3.2. Repetitive Guidance Module

Depth in challenging environments is not only extremely sparse but also diverse. Most of the existing methods suffer from unclear structures, especially near the object boundaries. Since gradual refinement is proven effective [3, 35, 47] to tackle this issue, we propose our repetitive guidance module to progressively generate dense and structure-detailed depth maps. As shown in Fig. 2, our depth generation branch has the same architecture as  $RHN_1$ . Given the sparse depth input and color image guidance features  $D_{ij}$  in the decoder of the last RHN, our depth branch generates final dense predictions. At the stage of the depth branch's encoder, our repetitive guidance module (left of Fig. 3) takes  $D_{ij}$  and  $e_{1j}$  as input and employs the efficient guidance algorithm (in Sec. 3.2.1) to produce refined depth  $d_{jk}$  step by step. Then we fuse the refined  $d_{jk}$  by our adaptive fusion mechanism (in Sec. 3.2.2), obtaining the depth  $d_j$ . We define the process as:

$$d_j = RG(D_{ij}, e_{1j}), \quad (2)$$

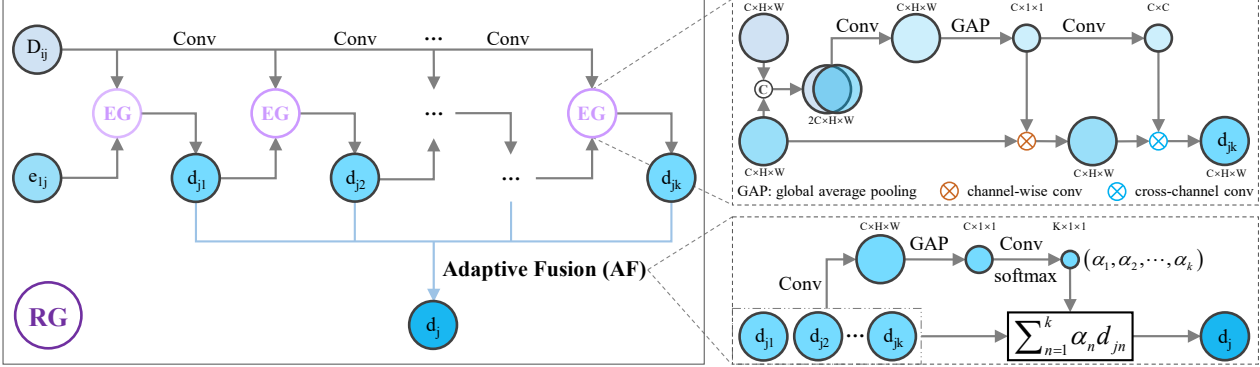


Figure 3. Our repetitive guidance module (RG) implemented by an adaptive fusion mechanism (AF) and an efficient guidance algorithm (EG). Conv means convolution and  $k$  refers to the repetitive number.

where  $RG(\cdot)$  refers to the repetitive guidance function.

### 3.2.1 Efficient Guidance Algorithm

Suppose the size of inputs  $D_{ij}$  and  $e_{1j}$  are both  $C \times H \times W$ . It is easy to figure out the complexity of the dynamic convolution is  $O(C \times C \times R^2 \times H \times W)$ , which generates spatial-variant kernels according to color image features.  $R^2$  is the size of the filter kernel window. In fact,  $C$ ,  $H$ , and  $W$  are usually very large, it's thus necessary to reduce the complexity of the dynamic convolution. GuideNet [42] proposes channel-wise and cross-channel convolution factorization, whose complexity is  $O(C \times R^2 \times H \times W + C \times C)$ . However, our repetitive guidance module employs the convolution factorization many times, where the channel-wise process still needs massive GPU memory consumption, which is  $O(C \times R^2 \times H \times W)$ . As a result, inspired by SENet [15] that captures high-frequency response with channel-wise differentiable operations, we design an efficient guidance unit to simultaneously reduce the complexity of the channel-wise convolution and encode high-frequency components, which is shown in the top right of Fig. 3. Specifically, we first concatenate the image and depth inputs and then conduct a  $3 \times 3$  convolution. Next, we employ the global average pooling function to generate a  $C \times 1 \times 1$  feature. At last, we perform pixel-wise dot between the feature and the depth input. The complexity of our channel-wise convolution is only  $O(C \times H \times W)$ , reduced to  $1/R^2$ . The process is defined as:

$$d_{jk} = \begin{cases} EG(D_{ij}, e_{1j}), & k = 1, \\ EG(Conv(D_{ij}), d_{k-1}), & k > 1, \end{cases} \quad (3)$$

where  $EG(\cdot)$  represents the efficient guidance function.

Suppose the memory consumptions of the common dynamic convolution, convolution factorization, and ours are

| Method       | dynamic convolution | convolution factorization | our EG |
|--------------|---------------------|---------------------------|--------|
| Memory (GB)  | 42.75               | 0.334                     | 0.037  |
| Times (-/EG) | 1155                | 9                         | 1      |

Table 1. GPU memory consumption of different methods, including the dynamic convolution, convolution factorization [42], and our efficient guidance algorithm (EG).

$M_{DC}$ ,  $M_{CF}$ , and  $M_{AG}$  respectively. Then,

$$\begin{aligned} \frac{M_{EG}}{M_{DC}} &= \frac{C \times H \times W + C \times C}{C \times C \times R^2 \times H \times W} \\ &= \frac{1}{C \times R^2} + \frac{1}{H \times W \times R^2}, \end{aligned} \quad (4)$$

and

$$\begin{aligned} \frac{M_{EG}}{M_{CF}} &= \frac{C \times H \times W + C \times C}{C \times R^2 \times H \times W + C \times C} \\ &= \frac{H \times W + C}{H \times W \times R^2 + C}. \end{aligned} \quad (5)$$

Under the setting of the second fusion stage in our depth branch, using 4-byte floating precision and taking  $C = 128$ ,  $H = 128$ ,  $W = 608$ , and  $R = 3$ , as shown in Table 1, the GPU memory of our efficient guidance algorithm is reduced from 42.75GB to 0.037GB compared with the common dynamic convolution, nearly 1155 times lower for one fusion stage. Compared to the convolution factorization in GuideNet [42], the GPU memory of ours is reduced from 0.334GB to 0.037GB, nearly 9 times lower. Therefore, we can conduct our repetitive strategy easily without worrying much about GPU memory consumption based on the pipeline of GuideNet.

### 3.2.2 Adaptive Fusion Mechanism

Since many coarse depth features ( $d_{j1}, d_{j2}, \dots, d_{jk}$ ) are available in our repetitive guidance module, it comes naturally to jointly utilize them to generate refined depth maps, which has been proved effective in various related methods [53, 27, 3, 40, 35, 16]. Inspired by the selective kernel convolution in SKNet [26], we propose the adaptive

fusion mechanism to refine depth, which is illustrated in the bottom right of Fig. 3. Specifically, given inputs  $(d_{j1}, d_{j2}, \dots, d_{jk})$ , we first concatenate them and then perform a  $3 \times 3$  convolution. Next, the global average pooling function is employed to obtain a  $C \times 1 \times 1$  feature map. Another  $3 \times 3$  convolution and a softmax function are applied, obtaining  $(\alpha_1, \alpha_2, \dots, \alpha_k)$ :

$$\alpha_k = \text{Soft}(\text{Conv}(\text{GAP}(\text{Conv}(d_{j1} || d_{j2} || \dots || d_{jk})))), \quad (6)$$

where  $\text{Soft}(\cdot)$  and  $||$  refer to softmax function and concatenation.  $\text{GAP}(\cdot)$  represents the global average pooling operation. Finally, we fuse the  $k$  coarse depth maps using  $\alpha_k$  to produce the output  $d_j$ :

$$d_j = \sum_{n=1}^k \alpha_n d_{jn}. \quad (7)$$

The Eqs. 6 and 7 can be denoted as:

$$d_j = \text{AF}(d_{j1}, d_{j2}, \dots, d_{jk}), \quad (8)$$

where  $\text{AF}(\cdot)$  represents the adaptive fusion function.

## 4. RigNet

In this section, we describe the network architecture and the loss function for training. The proposed RigNet mainly consists of two parts: (1) a color image guidance branch for the generation of higher-level and clear semantics based on the repetitive hourglass network, and (2) a depth generation branch for structure-detailed depth predictions based on the novel repetitive guidance module with an efficient guidance algorithm and an adaptive fusion mechanism. Note that we give a potential explanation why image guided methods can work from the feature level in the supplementary material.

### 4.1. Network Architecture

In Fig. 2, we provide an overview of our network. In our color image branch, the  $\text{RHN}_1$  encoder-decoder unit is built upon residual networks [14]. In addition, we adopt the common feature connection strategy [38, 2] to simultaneously utilize low-level and high-level features.  $\text{RHN}_i$  ( $i > 1$ ) has the same architecture with  $\text{RHN}_1$ , which is used to extract clearer image guidance semantics [49].

The structure of depth generation branch is the same as  $\text{RHN}_1$ . In this branch, we perform repetitive guidance module based on dynamic convolution to gradually produce structure-detailed depth features at multiple stages, which is shown in Fig. 3 and described in Sec. 3.2. Detailed differences between our efficient guidance algorithm and the convolution factorization proposed in GuideNet [42], can be found in the supplementary material.

## 4.2. Loss Function

During training, we adopt the mean squared error (MSE) to compute the loss between ground truth annotations and depth predictions. In real world, the ground truth depth is often semi-dense, which is limited by existing technologies. Thus, following previous works, we compute the training loss only at the valid pixels in the reference ground truth depth maps. The final loss function is:

$$\mathcal{L} = \frac{1}{m} \sum_{q \in Q_v} \|GT_q - P_q\|^2, \quad (9)$$

where  $GT$  and  $P$  refer to ground truth depth and predicted depth respectively.  $Q_v$  represents the set of valid pixels in  $GT$ ,  $m$  is the number of the valid pixels.

## 5. Experiments

In this section, we first introduce the related datasets, metrics and implementation details. Then, we conduct extensive experiments to evaluate the performance of our method against other state-of-the-art approaches on public available datasets. Finally, a number of ablation studies are employed to verify the effectiveness of our method.

### 5.1. Datasets

**KITTI Depth Completion Dataset.** The KITTI depth completion benchmark is a large self-driving real-world dataset with street views from a driving vehicle [43]. It consists of 86,898 ground truth annotations with aligned sparse LiDAR maps and color images for training, 7,000 frames for validation, and another 1,000 frames for testing. The official 1,000 validation images are used during training while the remained images are ignored. The sparse depth maps are obtained by projecting the raw LiDAR points through the view of camera. The ground truth denser depth maps are generated by first projecting the accumulated LiDAR scans of multiple timestamps, and then removing abnormal depth values from occlusion and moving objects via comparing with stereo depths from image pairs. Since there are rare LiDAR points at the top of depth maps, the input images are bottom center cropped to  $1216 \times 256$  for training and testing [44, 42].

**NYUv2 Dataset.** The NYUv2 dataset [39] is comprised of video sequences from a variety of indoor scenes as recorded by both the color and depth cameras from the Microsoft Kinect. It consists of color images and depth images in 464 indoor scenes captured by Microsoft Kinect sensors. Following previous depth completion methods [32, 2, 37, 35, 42], we train our model on 50K images from the official training split, and test on the 654 images from the official labeled test set. Each image is downsized to  $320 \times 240$ , and then  $304 \times 228$  center-cropping is applied.

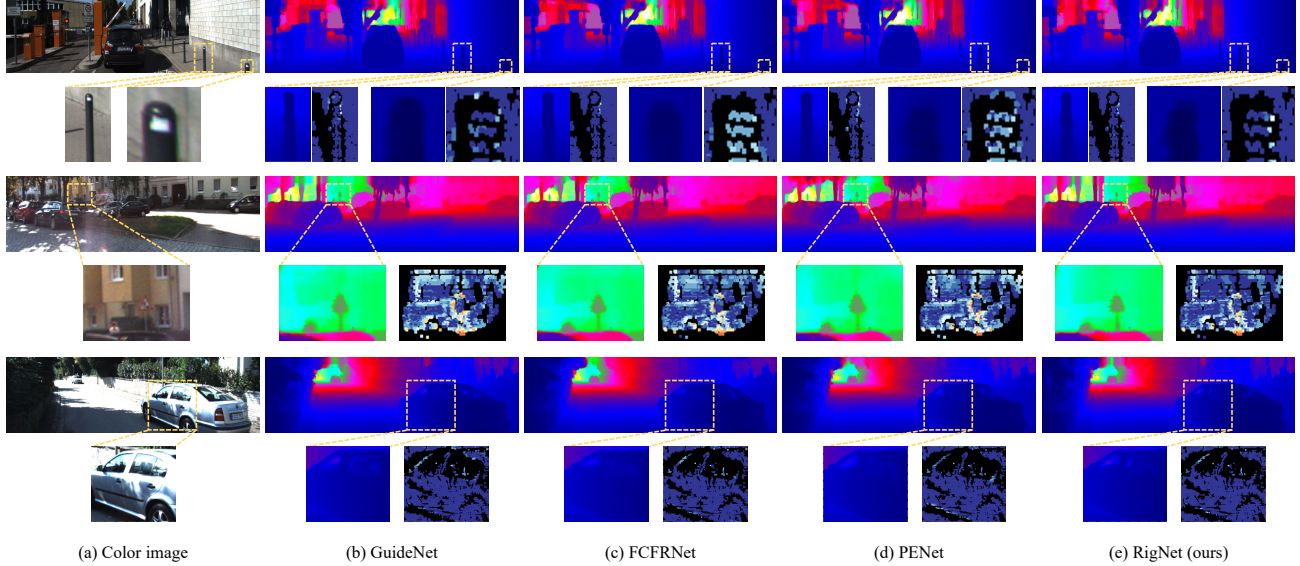


Figure 4. Qualitative comparisons with state-of-the-art methods on KITTI depth completion test set, including (b) GuideNet [42], (c) FCFRNet [28], and PENet [16]. Given sparse depth maps and the aligned color images (1st column), depth completion models output dense depth predictions (e.g., 2nd column). We provide error maps borrowed from the KITII leaderboard for detailed discrimination. Warmer color in error maps refer to higher error.

As the input resolution of our network must be a multiple of 32, we further pad the images to  $320 \times 256$ , but evaluate only at the valid region of size  $304 \times 228$  to keep fair comparison with other methods.

## 5.2. Metrics

For outdoor KITTI depth completion dataset, following the KITTI benchmark and existing methods [32, 37, 35, 42, 28, 16], we use four standard metrics for evaluation: root mean squared error (RMSE), mean absolute error (MAE), root mean squared error of the inverse depth (iRMSE), and mean absolute error of the inverse depth (iMAE), where RMSE is chosen as the dominant metric.

For indoor NYUv2 dataset, following previous works [2, 37, 35, 42, 28], three metrics are selected for evaluation: RMSE, mean absolute relative error (REL), and  $\delta_i$  which means the percentage of predicted pixels whose relative error is less a threshold  $i$  ( $1.25$ ,  $1.25^2$ , and  $1.25^3$ ). Higher  $i$  indicates a softer constraint and higher  $\delta_i$  represents more accurate predictions.

## 5.3. Implementation Details

Our method is implemented on the Pytorch [36] framework, and is particularly trained with 4 TITAN RTX GPUs. The training setting is similar with GuideNet [42]. We train our model for 20 epochs with the loss defined in Eq. 9. We use ADAM [22] as the optimizer with the momentum of  $\beta_1 = 0.9$ ,  $\beta_2 = 0.999$ , a starting learning rate of  $1 \times 10^{-3}$ , and weight decay of  $1 \times 10^{-6}$ . The learning rate drops by half every 5 epochs. The synchronized cross-GPU batch normalization [20, 50] is used when training.

| Method        | RMSE<br>mm    | MAE<br>mm     | iRMSE<br>1/km | iMAE<br>1/km | reference |
|---------------|---------------|---------------|---------------|--------------|-----------|
| CSPN [4]      | 1019.64       | 279.46        | 2.93          | 1.15         | ECCV18    |
| From [31]     | 901.43        | 292.36        | 4.92          | 1.35         | CVPR20    |
| TWISE [18]    | 840.20        | <b>195.58</b> | 2.08          | <b>0.82</b>  | CVPR21    |
| NConv [9]     | 829.98        | 233.26        | 2.60          | 1.03         | PAMI20    |
| S2D [32]      | 814.73        | 249.95        | 2.80          | 1.21         | ICRA19    |
| PwP [46]      | 777.05        | 235.17        | 2.42          | 1.13         | ICCV19    |
| Fusion [44]   | 772.87        | 215.02        | 2.19          | 0.93         | MVA19     |
| DSPN [47]     | 766.74        | 220.36        | 2.47          | 1.03         | ICIP20    |
| DLiDAR [37]   | 758.38        | 226.50        | 2.56          | 1.15         | CVPR19    |
| FuseNet [2]   | 752.88        | 221.19        | 2.34          | 1.14         | ICCV19    |
| ACMNet [54]   | 744.91        | 206.09        | 2.08          | 0.90         | TIP21     |
| CSPN++ [3]    | 743.69        | 209.28        | 2.07          | 0.90         | AAAI20    |
| NLSPN [35]    | 741.68        | 199.59        | <b>1.99</b>   | 0.84         | ECCV20    |
| GuideNet [42] | 736.24        | 218.83        | 2.25          | 0.99         | TIP20     |
| FCFRNet [28]  | 735.81        | 217.15        | 2.20          | 0.98         | AAAI21    |
| PENet [16]    | 730.08        | 210.55        | 2.17          | 0.94         | ICRA21    |
| RigNet (ours) | <b>713.44</b> | 204.55        | 2.16          | 0.92         | -         |

Table 2. Quantitative comparisons with state-of-the-art methods on KITTI depth completion benchmark. Best results are shown in bold. The results of other methods are obtained from the **KITTI leaderboard**, ranked by the RMSE. We rank 1st on the leaderboard at the time of submission.

## 5.4. Evaluation on KITTI Dataset

Table 2 shows the quantitative results of our method and other approaches on the KITTI benchmark, whose dominant evaluation metric is the RMSE. Our RigNet ranks 1st on the leaderboard at the time of submission, outperform-

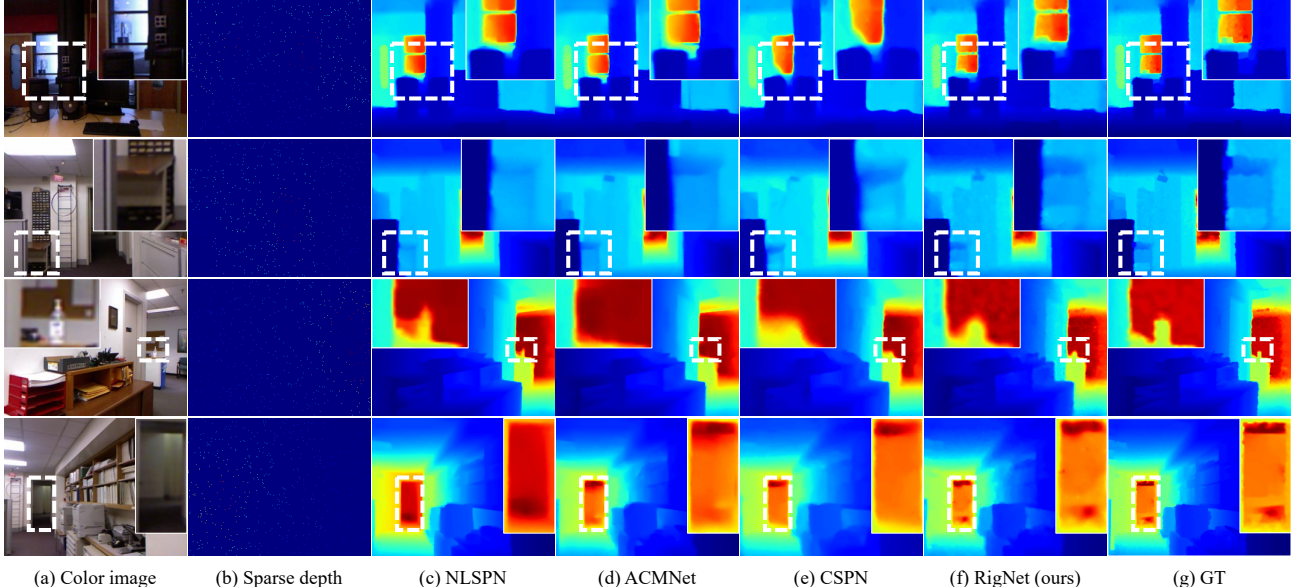


Figure 5. Qualitative comparisons with state-of-the-art methods on NYUv2 test set. From left to right: (a) color image, (b) sparse depth, (c) NLSPN [35], (d) ACMNet [54], (e) CSPN [4], (f) our RigNet, and (g) ground truth. We present the results of these four methods under 500 samples. The circled rectangle areas show the recovery of object details. Best viewed in color.

ing the 2nd with significant 17mm improvement while the errors of other state-of-the-art works are very closed. Here, our RigNet is also better than those approaches that employ additional dataset, *e.g.*, DLiDAR [37] utilizes CARLA [8] to predict surface normals for better depth predictions. Qualitative comparisons with several state-of-the-art works are shown in Fig. 4. While all methods provide visually good results in general, our estimated depth maps possess more details and more accurate object boundaries. The corresponding error maps can offer supports more clearly. For example, among the marked iron pillars in the first row of Fig. 4, the error of our prediction is significantly smaller than the others. More visualization results are in the supplementary material.

## 5.5. Evaluation on NYUv2 Dataset

To verify the performance of proposed method on indoor scenes, following existing approaches [3, 35, 42, 28], we train our repetitive image guided network on the NYUv2 dataset [39] with the setting 500 sparse samples. As illustrated in Table 3, our model achieves the best performance among all traditional and latest approaches without using additional datasets, which proves that our network possesses stronger generalization capability. Fig. 5 demonstrates the qualitative visualization results. Obviously, compared with those state-of-the-art methods, our RigNet can recover more detailed structures with lower errors at most pixels, including sharper boundaries and more complete object shapes. For example, among the marked doors in the last row of Fig. 5, our prediction is very close to the ground truth, while others either have large errors in the whole re-

| Method                | RMSE<br>m    | REL<br>m     | $\delta_{1.25}$ | $\delta_{1.25^2}$ | $\delta_{1.25^3}$ | reference |
|-----------------------|--------------|--------------|-----------------|-------------------|-------------------|-----------|
| TGV [10]              | 0.635        | 0.123        | 81.9            | 93.0              | 96.8              | ICCV13    |
| Bilateral [39]        | 0.479        | 0.084        | 92.4            | 97.6              | 98.9              | ECCV12    |
| Zhang [51]            | 0.228        | 0.042        | 97.1            | 99.3              | 99.7              | CVPR18    |
| S2D_18 [33]           | 0.230        | 0.044        | 97.1            | 99.4              | 99.8              | ICRA18    |
| DCoeff [19]           | 0.118        | 0.013        | 99.4            | <b>99.9</b>       | -                 | CVPR19    |
| CSPN [4]              | 0.117        | 0.016        | 99.2            | <b>99.9</b>       | <b>100.0</b>      | ECCV18    |
| CSPN++ [3]            | 0.116        | -            | -               | -                 | -                 | AAAI20    |
| DLiDAR [37]           | 0.115        | 0.022        | 99.3            | <b>99.9</b>       | <b>100.0</b>      | CVPR19    |
| Xu <i>et al.</i> [46] | 0.112        | 0.018        | 99.5            | <b>99.9</b>       | <b>100.0</b>      | ICCV19    |
| FCFRNet [28]          | 0.106        | 0.015        | 99.5            | <b>99.9</b>       | <b>100.0</b>      | AAAI21    |
| ACMNet [54]           | 0.105        | 0.015        | 99.4            | <b>99.9</b>       | <b>100.0</b>      | TIP21     |
| PRNet [24]            | 0.104        | 0.014        | 99.4            | <b>99.9</b>       | <b>100.0</b>      | CVPR21    |
| GuideNet [42]         | 0.101        | 0.015        | 99.5            | <b>99.9</b>       | <b>100.0</b>      | TIP20     |
| TWISE [18]            | 0.097        | 0.013        | <b>99.6</b>     | <b>99.9</b>       | <b>100.0</b>      | CVPR21    |
| NLSPN [35]            | 0.092        | <b>0.012</b> | <b>99.6</b>     | <b>99.9</b>       | <b>100.0</b>      | ECCV20    |
| RigNet (ours)         | <b>0.090</b> | 0.013        | <b>99.6</b>     | <b>99.9</b>       | <b>100.0</b>      | -         |

Table 3. Quantitative comparisons with different methods on the NYUv2 dataset. Best results are shown in bold. We compare to traditional algorithms [10, 39] and various deep learning based approaches. Our RigNet outperforms the latest state-of-the-art methods [35, 42, 28, 54] when considering the main RMSE metric.

gions or have blurry shapes on specific objects.

## 5.6. Ablation Studies

In this section, we employ extensive experiments to verify the effectiveness of each component proposed in our method, including the repetitive hourglass network (RHN)

| Method   | RHN              |                  |                  | RG             |                 |                 |                 | AF  |        |      | GPU memory<br>GB | RMSE<br>mm   |
|----------|------------------|------------------|------------------|----------------|-----------------|-----------------|-----------------|-----|--------|------|------------------|--------------|
|          | RHN <sub>1</sub> | RHN <sub>2</sub> | RHN <sub>3</sub> | G <sub>1</sub> | EG <sub>1</sub> | EG <sub>2</sub> | EG <sub>3</sub> | add | concat | ours |                  |              |
| baseline | ✓                |                  |                  | ✓              |                 |                 |                 |     |        |      | -5.99            | 778.6        |
| (a)      | ✓                | ✓                |                  |                | ✓               |                 |                 |     |        |      | ±0               | 771.7        |
| (b)      | ✓                | ✓                | ✓                |                | ✓               |                 |                 |     |        |      | +5.98            | 769.4        |
| (c)      | ✓                | ✓                |                  |                | ✓               |                 |                 |     |        |      | -11.95           | 768.6        |
| (d)      | ✓                | ✓                |                  |                | ✓               | ✓               |                 |     |        |      | -0.05            | 762.3        |
| (e)      | ✓                | ✓                |                  |                | ✓               | ✓               | ✓               |     |        |      | +11.87           | 757.4        |
| (f)      | ✓                | ✓                |                  |                | ✓               | ✓               | ✓               | ✓   |        |      | +11.87           | 755.8        |
| (g)      | ✓                | ✓                |                  |                | ✓               | ✓               | ✓               |     | ✓      |      | +11.86           | 754.6        |
| (h)      | ✓                | ✓                |                  |                | ✓               | ✓               | ✓               |     |        | ✓    | +11.73           | <b>752.1</b> |

Table 4. Ablation studies of depth completion on KITTI validation set. RHN: repetitive hourglass network. RG: repetitive guidance module. EG: efficient guidance algorithm. AF: adaptive fusion mechanism. RHN<sub>i</sub> and RG-EG<sub>k</sub> refer to the case where we repeatedly use them *i* and *k* times respectively. G<sub>1</sub> represents the raw guided convolution in GuideNet [42], which is used only once in one fusion stage. When performing method (h), our model achieves the lowest error.

and the repetitive guidance module (RG), which consists of an efficient guidance algorithm (EG) and an adaptive fusion mechanism (AF). Corresponding experimental results are listed in Table 4. Note that the batch size is set to 8 when computing the GPU memory consumption.

#### Effect of Repetitive Hourglass Network.

The state-of-the-art baseline GuideNet [42] employs a simple U-net based on Resnets and an interesting guided convolution module G<sub>1</sub> to predict dense depth. On this basis, we repeatedly conduct our RHN twice (a) and thrice (b). In contrast, as shown in Table 4, the errors of (a) and (b) are 6.9mm and 9.2mm lower than that of the baseline, respectively. These facts indicate that our RHN design has stronger feature extraction ability in challenging regions, providing clearer image guidance for our depth generation branch. In general, the depth values will be more accurate as the repetition number increases. It can be found in Table 4 that one RHN approximately consumes 6GB GPU memory. Therefore, we choose to perform RHN<sub>2</sub> in following experiments when considering the trade-off between the accuracy and the GPU memory consumption.

#### Effect of Repetitive Guidance Module.

**(i) Efficient Guidance.** Note that we directly output the features in EG<sub>3</sub> when not employing AF. Table 1 and Equations 4, 5 have provided quantitative analysis in theory for our EG design. Based on (a), we disable G<sub>1</sub> by replacing it with our EG<sub>1</sub>. Comparing (c) with (a) in Table 4, both of which carry out the guided convolution technology only once, although the error of (c) goes down a little bit, the GPU memory consumption is heavily reduced by 11.95GB. These results give strong evidence that our new guidance design is not only effective but also efficient.

**(ii) Repetitive Guidance.** When the recursion number *k* of EG increases, due to the continuous extraction of high-frequency components (*e.g.*, object boundaries), the errors of (d) and (e) are 6.3mm and 11.2mm significantly lower than that of (c) respectively, which forcefully show the ef-

fectiveness of our repetitive guidance design. In addition, the GPU memory consumption of RG-EG<sub>3</sub> is less than that of (a). Note that, GuideNet and our RigNet both have four fusion stages, thus the number of EG will rise to 4*k* when replacing G<sub>1</sub> with RG-EG<sub>k</sub>. For example, when conducting RG-EG<sub>2</sub>, (d)'s GPU memory consumption is almost equal to that of (a) as the number of EG is 8. Such numerical result is consistent with Eq. 5 and the instance below it.

**(iii) Adaptive Fusion.** Based on (e) that directly outputs the feature of RG-EG<sub>3</sub>, we choose to utilize all features of RG-EG<sub>*k*</sub> (*k* = 1, 2, 3) to produce better depth representations. (f), (g), and (h) refer to addition, concatenation, and our AF strategies, respectively. Specifically in (g), we conduct a 3 × 3 convolution to control the channel to be the same as RG-EG<sub>3</sub>'s after concatenation. As we can see in Table 4, all of the three strategies improve the performance of the model with a little bit GPU memory sacrifice (about 0-0.14GB), which demonstrates that aggregating multi-step features in repetitive procedure is effective. Furthermore, our AF mechanism obtains the best result among the three strategies, outperforming (e) 5.3mm. The above facts prove that our AF design benefits the system better than those simple fusion strategies. Detailed difference of intermediate features produced by our repetitive design can be found in Fig. 1 and the supplementary material.

## 6. Conclusion

In this paper, we explored a novel repetitive design in our image guided network for depth completion. We pointed out that there were two issues impeding the performance of existing outstanding methods, *i.e.*, the fuzzy image guidance and object structures in depth. To tackle the former issue, in our image guidance branch, we presented a novel repetitive hourglass network to produce clearer image guidance via repeatedly stacking hourglass units. To alleviate the latter issue, in our depth generation branch, we designed

a repetitive guidance module to gradually predict structure-detailed depth maps. Meanwhile, to model high-frequency components and reduce GPU memory consumption of the module, we proposed an efficient guidance algorithm to dynamically encode depth features. Furthermore, we designed an adaptive fusion mechanism to automatically fuse multi-step depth features for better predictions. Extensive experiments show that our method achieves state-of-the-art performance on both the indoor and outdoor datasets.

## References

- [1] Claudia Armbrüster, Marc Wolter, Torsten Kuhlen, Will Spijkers, and Bruno Fimm. Depth perception in virtual reality: distance estimations in peri-and extrapersonal space. *Cyberpsychology & Behavior*, 11(1):9–15, 2008. [1](#)
- [2] Yun Chen, Bin Yang, Ming Liang, and Raquel Urtasun. Learning joint 2d-3d representations for depth completion. In *ICCV*, pages 10023–10032, 2019. [1, 2, 5, 6](#)
- [3] Xinjing Cheng, Peng Wang, Chenye Guan, and Ruigang Yang. Cspn++: Learning context and resource aware convolutional spatial propagation networks for depth completion. In *AAAI*, pages 10615–10622, 2020. [2, 3, 4, 6, 7](#)
- [4] Xinjing Cheng, Peng Wang, and Ruigang Yang. Learning depth with convolutional spatial propagation network. In *ECCV*, pages 103–119, 2018. [2, 6, 7](#)
- [5] Nathaniel Chodosh, Chaoyang Wang, and Simon Lucey. Deep convolutional compressed sensing for lidar depth completion. In *ACCV*, pages 499–513, 2018. [2](#)
- [6] Zhaopeng Cui, Lionel Heng, Ye Chuan Yeo, Andreas Geiger, Marc Pollefeys, and Torsten Sattler. Real-time dense mapping for self-driving vehicles using fisheye cameras. In *ICRA*, pages 6087–6093, 2019. [1](#)
- [7] Arindam Dey, Graeme Jarvis, Christian Sandor, and Gerhard Reitmayr. Tablet versus phone: Depth perception in handheld augmented reality. In *ISMAR*, pages 187–196, 2012. [1](#)
- [8] Alexey Dosovitskiy, German Ros, Felipe Codevilla, Antonio Lopez, and Vladlen Koltun. Carla: An open urban driving simulator. In *CoRL*, pages 1–16. PMLR, 2017. [7](#)
- [9] Abdelrahman Elde索key, Michael Felsberg, and Fahad Shahbaz Khan. Confidence propagation through cnns for guided sparse depth regression. *IEEE Transactions on Pattern Analysis and Machine Intelligence*, 42(10):2423–2436, 2020. [1, 2, 6](#)
- [10] David Ferstl, Christian Reinbacher, Rene Ranftl, Matthias Rüther, and Horst Bischof. Image guided depth upsampling using anisotropic total generalized variation. In *ICCV*, pages 993–1000, 2013. [7](#)
- [11] Ruohan Gao, Changan Chen, Ziad Al-Halah, Carl Schissler, and Kristen Grauman. Visualechoes: Spatial image representation learning through echolocation. In *ECCV*, pages 658–676. Springer, 2020. [1](#)
- [12] Golnaz Ghiasi, Tsung-Yi Lin, and Quoc V Le. Nas-fpn: Learning scalable feature pyramid architecture for object detection. In *CVPR*, pages 7036–7045, 2019. [2](#)
- [13] Christian Häne, Lionel Heng, Gim Hee Lee, Friedrich Fraundorfer, Paul Furgale, Torsten Sattler, and Marc Pollefeys. 3d visual perception for self-driving cars using a multi-camera system: Calibration, mapping, localization, and obstacle detection. *Image and Vision Computing*, 68:14–27, 2017. [1](#)
- [14] Kaiming He, Xiangyu Zhang, Shaoqing Ren, and Jian Sun. Deep residual learning for image recognition. In *CVPR*, pages 770–778, 2016. [2, 5](#)
- [15] Jie Hu, Li Shen, and Gang Sun. Squeeze-and-excitation networks. In *CVPR*, pages 7132–7141, 2018. [4](#)
- [16] Mu Hu, Shuling Wang, Bin Li, Shiyu Ning, Li Fan, and Xiaojin Gong. Penet: Towards precise and efficient image guided depth completion. *arXiv preprint arXiv:2103.00783*, 2021. [1, 2, 3, 4, 6](#)
- [17] Yu-Kai Huang, Tsung-Han Wu, Yueh-Cheng Liu, and Winston H Hsu. Indoor depth completion with boundary consistency and self-attention. In *ICCV Workshops*, pages 0–0, 2019. [2](#)
- [18] Saif Imran, Xiaoming Liu, and Daniel Morris. Depth completion with twin surface extrapolation at occlusion boundaries. In *CVPR*, pages 2583–2592, 2021. [6, 7](#)
- [19] Saif Imran, Yunfei Long, Xiaoming Liu, and Daniel Morris. Depth coefficients for depth completion. In *CVPR*, pages 12438–12447. IEEE, 2019. [7](#)
- [20] Sergey Ioffe and Christian Szegedy. Batch normalization: Accelerating deep network training by reducing internal covariate shift. In *ICML*, pages 448–456. PMLR, 2015. [6](#)
- [21] Maximilian Jaritz, Raoul De Charette, Emilie Wirbel, Xavier Perrotton, and Fawzi Nashashibi. Sparse and dense data with cnns: Depth completion and semantic segmentation. In *3DV*, pages 52–60, 2018. [2](#)
- [22] Diederik P Kingma and Jimmy Ba. Adam: A method for stochastic optimization. In *Computer Ence*, 2014. [6](#)
- [23] Jason Ku, Ali Harakeh, and Steven L Waslander. In defense of classical image processing: Fast depth completion on the cpu. In *CRV*, pages 16–22, 2018. [2](#)
- [24] Byeong-Uk Lee, Kyunghyun Lee, and In So Kweon. Depth completion using plane-residual representation. In *CVPR*, pages 13916–13925, 2021. [7](#)
- [25] Ang Li, Zejian Yuan, Yonggen Ling, Wanchao Chi, Chong Zhang, et al. A multi-scale guided cascade hourglass network for depth completion. In *WACV*, pages 32–40, 2020. [2](#)
- [26] Xiang Li, Wenhui Wang, Xiaolin Hu, and Jian Yang. Selective kernel networks. In *CVPR*, pages 510–519, 2019. [4](#)
- [27] Tsung-Yi Lin, Piotr Dollár, Ross Girshick, Kaiming He, Bharath Hariharan, and Serge Belongie. Feature pyramid networks for object detection. In *CVPR*, pages 2117–2125, 2017. [4](#)
- [28] Lina Liu, Xibin Song, Xiaoyang Lyu, Junwei Diao, Mengmeng Wang, Yong Liu, and Liangjun Zhang. Fcfr-net: Feature fusion based coarse-to-fine residual learning for monocular depth completion. *arXiv preprint arXiv:2012.08270*, 2020. [1, 2, 6, 7](#)
- [29] Shu Liu, Lu Qi, Haifang Qin, Jianping Shi, and Jiaya Jia. Path aggregation network for instance segmentation. In *CVPR*, pages 8759–8768, 2018. [2](#)

[30] Kaiyue Lu, Nick Barnes, Saeed Anwar, and Liang Zheng. From depth what can you see? depth completion via auxiliary image reconstruction. In *CVPR*, pages 11306–11315, 2020. 2

[31] Kaiyue Lu, Nick Barnes, Saeed Anwar, and Liang Zheng. From depth what can you see? depth completion via auxiliary image reconstruction. In *CVPR*, pages 11306–11315, 2020. 6

[32] Fangchang Ma, Guilherme Venturelli Cavalheiro, and Sertac Karaman. Self-supervised sparse-to-dense: Self-supervised depth completion from lidar and monocular camera. In *ICRA*, 2019. 1, 2, 5, 6

[33] Fangchang Ma and Sertac Karaman. Sparse-to-dense: Depth prediction from sparse depth samples and a single image. In *ICRA*, pages 4796–4803. IEEE, 2018. 7

[34] Kranti Kumar Parida, Siddharth Srivastava, and Gaurav Sharma. Beyond image to depth: Improving depth prediction using echoes. *arXiv preprint arXiv:2103.08468*, 2021. 1

[35] Jinsun Park, Kyungdon Joo, Zhe Hu, Chi-Kuei Liu, and In So Kweon. Non-local spatial propagation network for depth completion. In *ECCV*, 2020. 1, 2, 3, 4, 5, 6, 7

[36] Adam Paszke, Sam Gross, Soumith Chintala, Gregory Chanan, Edward Yang, Zachary DeVito, Zeming Lin, Alban Desmaison, Luca Antiga, and Adam Lerer. Automatic differentiation in pytorch. 2017. 6

[37] Jiaxiong Qiu, Zhaopeng Cui, Yinda Zhang, Xingdi Zhang, Shuaicheng Liu, Bing Zeng, and Marc Pollefeys. Deeplidar: Deep surface normal guided depth prediction for outdoor scene from sparse lidar data and single color image. In *CVPR*, pages 3313–3322, 2019. 1, 5, 6, 7

[38] Olaf Ronneberger, Philipp Fischer, and Thomas Brox. U-net: Convolutional networks for biomedical image segmentation. In *MICCAI*, pages 234–241. Springer, 2015. 2, 5

[39] Nathan Silberman, Derek Hoiem, Pushmeet Kohli, and Rob Fergus. Indoor segmentation and support inference from rgbd images. In *ECCV*, pages 746–760. Springer, 2012. 5, 7

[40] Xibin Song, Yuchao Dai, Dingfu Zhou, Liu Liu, Wei Li, Hongdong Li, and Ruigang Yang. Channel attention based iterative residual learning for depth map super-resolution. In *CVPR*, pages 5631–5640, 2020. 1, 4

[41] Mingxing Tan, Ruoming Pang, and Quoc V Le. Efficientdet: Scalable and efficient object detection. In *CVPR*, pages 10781–10790, 2020. 2

[42] Jie Tang, Fei-Peng Tian, Wei Feng, Jian Li, and Ping Tan. Learning guided convolutional network for depth completion. *IEEE Transactions on Image Processing*, 30:1116–1129, 2020. 1, 2, 4, 5, 6, 7, 8

[43] Jonas Uhrig, Nick Schneider, Lukas Schneider, Uwe Franke, Thomas Brox, and Andreas Geiger. Sparsity invariant cnns. In *3DV*, pages 11–20, 2017. 2, 5

[44] Wouter Van Gansbeke, Davy Neven, Bert De Brabandere, and Luc Van Gool. Sparse and noisy lidar completion with rgb guidance and uncertainty. In *MVA*, pages 1–6. IEEE, 2019. 1, 2, 5, 6

[45] Wouter Van Gansbeke, Davy Neven, Bert De Brabandere, and Luc Van Gool. Sparse and noisy lidar completion with rgb guidance and uncertainty. In *MVA*, pages 1–6, 2019. 2

[46] Yan Xu, Xinge Zhu, Jianping Shi, Guofeng Zhang, Hujun Bao, and Hongsheng Li. Depth completion from sparse lidar data with depth-normal constraints. In *ICCV*, pages 2811–2820, 2019. 6, 7

[47] Zheyuan Xu, Hongche Yin, and Jian Yao. Deformable spatial propagation networks for depth completion. In *ICIP*, pages 913–917. IEEE, 2020. 2, 3, 6

[48] Yanchao Yang, Alex Wong, and Stefano Soatto. Dense depth posterior (ddp) from single image and sparse range. In *CVPR*, pages 3353–3362, 2020. 2

[49] Matthew D Zeiler and Rob Fergus. Visualizing and understanding convolutional networks. In *ECCV*, pages 818–833. Springer, 2014. 1, 5

[50] Hang Zhang, Kristin Dana, Jianping Shi, Zhongyue Zhang, Xiaogang Wang, Ambrish Tyagi, and Amit Agrawal. Context encoding for semantic segmentation. In *CVPR*, pages 7151–7160, 2018. 6

[51] Yinda Zhang and Thomas Funkhouser. Deep depth completion of a single rgbd image. In *CVPR*, pages 175–185, 2018. 7

[52] Zhenyu Zhang, Zhen Cui, Chunyan Xu, Yan Yan, Nicu Sebe, and Jian Yang. Pattern-affinitive propagation across depth, surface normal and semantic segmentation. In *CVPR*, pages 4106–4115, 2019. 1

[53] Hengshuang Zhao, Jianping Shi, Xiaojuan Qi, Xiaogang Wang, and Jiaya Jia. Pyramid scene parsing network. In *CVPR*, pages 2881–2890, 2017. 4

[54] Shanshan Zhao, Mingming Gong, Huan Fu, and Dacheng Tao. Adaptive context-aware multi-modal network for depth completion. *IEEE Transactions on Image Processing*, 2021. 1, 2, 6, 7